Geochemistry, Geophysics, Geosystems®

RESEARCH ARTICLE
10.1029/2021GC010267

Key Points:

- Brucite abundant domains release a fluid with a lower silica content than antigorite-rich domains
- Reactive fluid flow can trigger dehydration
- Preexisting vein-like structures form pathways for a low silica fluid to generate near pure olivine veins

Correspondence to:

K. Huber,
konstantin.huber@fu-berlin.de

Citation:

Huber, K., Vrijmoed, J. C., & John, T. (2022). Formation of olivine veins by reactive fluid flow in a dehydrating serpentinite. *Geochemistry, Geophysics, Geosystems*, *23*, e2021GC010267. https://doi.org/10.1029/2021GC010267

Received 15 NOV 2021
Accepted 8 JUN 2022

Formation of Olivine Veins by Reactive Fluid Flow in a Dehydrating Serpentinite

K. Huber[1], J. C. Vrijmoed[1], and T. John[1]

[1]Freie Universität Berlin, Berlin, Germany

Abstract Many exposed high-pressure meta-serpentinites comprise a channelized network of olivine-rich veins that formed during dehydration at depth and allowed the fluid to escape from the dehydrating rock. While previous studies have shown that chemical heterogeneities in rocks can control the formation of olivine-enriched vein-like interconnected porosity networks on the sub-millimeter scale, it is still unclear how these networks evolve toward larger scales and develop nearly pure olivine veins. To explore this, we study the effect of reactive fluid flow on a dehydrating serpentinite. We use thermodynamic equilibrium calculations to investigate the effect of variations in the bulk silica content in serpentinites on the dehydration reaction of antigorite + brucite = olivine + fluid and the silica content of this fluid phase. Further, we develop a numerical model that combines the effects of intrinsic chemical heterogeneities with reactive transport with dissolved silica as metasomatic agent. Our model shows how reactive transport can lead to vein widening and olivine enrichment within a vein in an antigorite-rich matrix, such as observed in the veins of the Erro Tobbio meta-serpentinites. This is a critical step in the evolution toward larger-scale vein systems and in the evolution of dynamic porosity, as this step helps account for the chemical feedback between the dehydrating rock and the liberated fluid.

1. Introduction

Serpentinites represent the major fluid source within subducting oceanic plates and carry large amounts of water, stored in hydrous minerals, into subduction zones worldwide (e.g., Rüpke et al., 2004; Scambelluri et al., 1995; van Keken et al., 2011). Fully hydrated oceanic mantle can store up to 13 wt. % water, which is released in a series of dehydration reactions (e.g., Plümper et al., 2017; Rüpke et al., 2004; Ulmer & Trommsdorff, 1995). In turn, these released fluids have large effects on important geodynamic processes such as earthquakes (Hacker et al., 2003; Jung et al., 2004; Moreno et al., 2014) and arc magmatism (John et al., 2012; Mazza et al., 2020; Schmidt & Poli, 1998).

In more detail, dehydration reactions lead to densification of the solid slab, which, in turn, gives rise to the formation of fluid-filled porosity. Initially, this porosity forms on the sub-millimeter scale and is heterogeneously distributed in the rock (Figure 1a), as defined by the local bulk composition (Plümper et al., 2017). As dehydration continues, these first vein-like porosity structures connect and form a vein network (Figure 1b). Within these centimeter-scale veins, metamorphic olivine and porosity form by the breakdown of antigorite via an intermediate phyllosilicate phase (IPP, Plümper et al., 2017, Figure 1d) which leads to widening of the veins and increasing draining efficiency. Finally, the fluid escapes (Figure 1c) by the formation of either fracture-like (e.g., Herms et al., 2012; John et al., 2008; Padrón-Navarta et al., 2010; Spandler et al., 2011) or porosity wave-like fluid pathways (Chen et al., 2019; Connolly & Podladchikov, 2007; Miller et al., 2003; Piccoli et al., 2021; Skarbek & Rempel, 2016).

One of the key dehydration reactions occurring in hydrated slab mantle is the breakdown of brucite and antigorite to form olivine and an aqueous fluid phase (Ulmer & Trommsdorff, 1995). In partially dehydrated serpentinites, the emergence of metamorphic olivine after serpentine is used as an indicator that these domains underwent dehydration. Such olivine-rich dehydration structures are commonly observed in previously subducted high-pressure ophiolites, for example, the Cerro del Almirez massif in Spain (López Sánchez-Vizcaíno et al., 2005, 2009), in the Sanbagwa metamorphic belt in Japan (Fukumura et al., 2019) or in various locations in the Western Alps (Clément et al., 2020; Groppo & Compagnoni, 2007; Kempf et al., 2020; Scambelluri et al., 1991). In many cases, olivine enrichment in these rocks is associated with deformation structures such as mylonitic shear zones (Hermann et al., 2000) or pseudotachylites (Magott et al., 2020), but occasionally these rocks also contain an

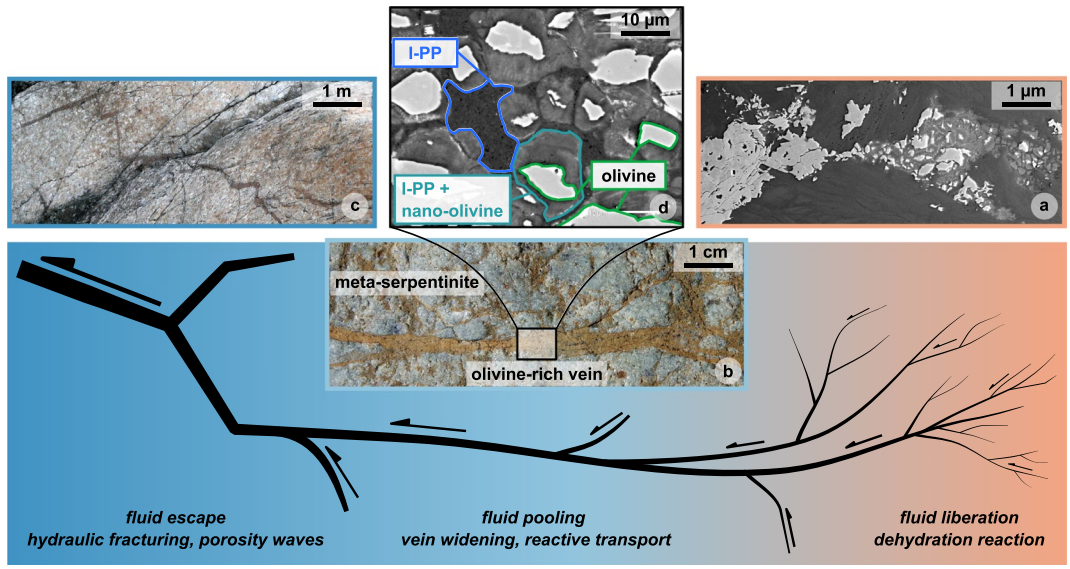

Figure 1. Channelized network of dehydration-related olivine-rich veins as observed in the Erro-Tobbio meta-serpentinites. Colors indicate the three main stages of rock dehydration on different length scales. The dominant processes acting on each scale are listed at the bottom. Arrows indicate the direction and magnitude of fluid flow in the veins. Panels (a–c) show the natural occurrence of olivine-rich veins on the µm-, the cm- and the m-scale, respectively. Panel (d) shows the mineral assemblage in an olivine-rich vein, displaying the reaction of intermediate phyllosilicate-phase (I-PP, Plümper et al. [2017]) to metamorphic olivine.

olivine-rich vein network in parts with only very little deformation. A key locality to study these olivine-rich veins is in the meta-serpentinites of the Erro Tobbio unit in the Ligurian Alps in Italy (Plümper et al., 2017; Scambelluri et al., 1991). These rocks show both olivine-rich mylonites and the olivine-rich vein network in an undeformed body of antigorite-rich country rock (Figures 1b and 1c).

As shown by Plümper et al. (2017), the formation of sub-millimeter vein-like porosity structures that are enriched in olivine (compared to the antigorite-rich surrounding matrix) are caused by intrinsic local variations in the bulk rock chemistry (Figure 1a), suggesting that dehydration leads to fluid channeling directly at the onset of the dehydration process. Such a dynamic vein network formation that eventually results in fluid release from the dehydrating rock volume has also been suggested, on the basis of measured variations in Vp/Vs ratios, in a seismological study of the slab mantle of the descending Nazca plate beneath Chile (Bloch et al., 2018). Further, magnetotelluric data derived from the Cascadia subduction zone imply that fluid flow from slabs is highly focused and directly feeds arc volcanoes (McGary et al., 2014). Along these lines, recent numerical studies (e.g., Cerpa et al., 2017; Wilson et al., 2014) have shown that on similarly large scales, compaction of mantle wedge rocks can also lead to fluid flow focusing. This type of fluid focusing also appears in geodynamic models: Models developed by Connolly (1997), Spiegelman et al. (2001), and Hesse et al. (2011) couple mineral reactions and solid deformation to show how melt flux in an uprising mantle section underneath a mid-ocean ridge localizes into meso-scale channels that feed the submarine volcanic systems. However, while these large-scale models offer important insights, they do not conceptually describe how the fluid flow mechanisms operate on the small scale, namely the scale at which dehydration reactions occur, nor do they indicate which mechanisms control and define the transition toward larger scales, such as the outcrop or plate scales. Accordingly, a key question remains: How do small-scale dehydrating systems, such as those described by Plümper et al. (2017), then further develop into near-pure olivine vein networks that occur on the outcrop scale (Figure 1, Scambelluri et al., 1995) and, thus, likely on even larger scales? This step is needed to derive a mechanistic understanding of how small-scale veins organize themselves on the larger scale to eventually form efficient fluid escape pathways that can drain the descending slab.

To understand this transition from the sub-millimeter scale studied by Plümper et al. (2017) to larger scales, one must consider the effects of reactive transport and, eventually, deformation. In the model by Plümper et al. (2017), the liberated fluid was treated as pure H_2O, and the chemistry of the liberated fluid and its interaction with the

wall rock system was not included in the dynamic modeling. However, changes in the fluid chemistry certainly feed back into the chemistry of the affected rock volume and, thus, may drive mineral reactions that consequently result in dehydration and, accordingly, a change in the mineral assemblage.

Therefore, in this work we extend the model of Plümper et al. (2017) by also considering silica dissolution and precipitation as well as transport of dissolved silica in the fluid phase. Here, we study the effects of reactive fluid flow on the development of the dehydration vein network in an undeformed serpentinite during dehydration of a subducting slab. In our model, we neglect compaction effects and gravity because the model deals with the local scale (millimeter to centimeter). Although compaction effects do become important at larger scales (decimeter to meter), where gravity plays an important role due to buoyancy effects, on this small scale compaction effects are assumed to have little influence on channelization. Our model shows how changes in the silica content of the fluid can lead to enhanced dehydration, vein widening, and olivine purification within the vein on the millimeter to centimeter scale. Starting from a non-porous rock, all porosity in our model is generated by dehydration mineral reactions first due to increasing temperature and then dynamically by subsequent reactive fluid flow.

2. Model Concept

2.1. Equations and Solution Strategy

The model is described by three balance laws for (a) total mass, (b) total silica mass and (c) non-volatile mass, that is, a chemical component that is present in the solid phase only and is not dissolved in the fluid phase. By substituting Darcy's law to describe fluid flow in the porous medium, assuming zero solid velocity ($v_s = 0$) and integrating over the non-volatile mass balance, these balance laws can be expressed in the form of Equations 1–3. The formulation of the reactive transport model follows the approach also used by Beinlich et al. (2020), here neglecting gravity due to the arguments outlined above. We consider SiO_2 to be dissolved in H_2O and also include transient fluid pressure evolution and its effect on mineral reactions as done in Plümper et al. (2017):

$$\frac{\partial\left(\rho_s\left(1-\phi\right)+\rho_f\phi\right)}{\partial t}=\nabla\cdot\left(\rho_f\frac{k_0\phi^3}{\mu}\nabla P_f\right) \tag{1}$$

$$\frac{\partial\left(\rho_s c_s\left(1-\phi\right)+\rho_f c_f\phi\right)}{\partial t}=\nabla\cdot\left(\rho_f c_f\frac{k_0\phi^3}{\mu}\nabla P_f+\rho_f c_f\phi D_c\nabla c_f\right) \tag{2}$$

$$\phi=1-\frac{\rho_s^0\left(1-c_s^0-X_h^0\right)\left(1-\phi^0\right)}{\rho_s\left(1-c_s-X_h\right)} \tag{3}$$

In total, these three equations contain seven unknowns: The fluid pressure (P_f), the SiO_2 content of the solid and the fluid (c_s and c_f, respectively), the H_2O content of the solid (X_h), porosity (ϕ) and the density of the solid and the fluid phase (ρ_s and ρ_f, respectively). D_c, k_0, and μ are the diffusivity of aqueous silica, the intrinsic solid permeability and the fluid viscosity, respectively, and are treated as constants. A superscript 0 denotes the initial value of that variable at time zero; the full list of variables and their units used in our model is also given in Table 1. Three of these variables (P_f, c_s, and ϕ) can be obtained by solving Equations 1–3, and the remaining four unknowns (ρ_s, ρ_f, X_h, and c_f) have been pre-computed and stored as functions of P_f and c_s in lookup tables from where they can be interpolated using the assumption of local equilibrium (Malvoisin et al., 2015; Plümper et al., 2017). Equations 1–3 were solved on a Cartesian grid using an explicit finite difference code with pseudo-transient iterations (e.g., Räss et al., 2019). The codes for the 1D and a 2D models as well as the lookup tables and the codes used to calculate them are available on Zenodo.

2.2. Scaling and Non-Dimensionalization

To reduce the number of independent physical parameters in our model, we used non-dimensional parameters. As independent parameters, we chose the diffusion constant D_c (m^2/s), length L (m), the fluid pressure P_f (Pa) and density ρ (kg/m^3). This choice allows one to express the time t and the permeability constant k_0/μ in dimensionless forms as $t^* = t\,D_c/L^2$ and $(k_0/\mu)^* = \frac{k_0 P_f}{\mu D_c}$, where * denotes the dimensionless parameter (Table 2).

Table 1
Notation Used in Our Model

Symbol	Meaning	Unit
ρ_s	Solid density	$kg \cdot m^{-3}$
ρ_s^0	Initial solid density at T_0	$kg \cdot m^{-3}$
ρ_f	Fluid density	$kg \cdot m^{-3}$
ϕ	Porosity	Dimensionless (volume fraction)
ϕ^0	Initial porosity at T_0	Dimensionless (volume fraction)
c_f	SiO_2 content of fluid	Dimensionless (weight fraction)
c_s	SiO_2 content of solid	Dimensionless (weight fraction)
c_s^0	Initial SiO_2 content of solid at T_0	Weight fraction
X_h	H_2O content of solid	Dimensionless (weight fraction)
X_h^0	Initial H_2O content of solid at T_0	Weight fraction
P_f	Fluid pressure	GPa
P_f^0	Initial fluid pressure	GPa
D_c	Diffusion constant	$m^2 \cdot s^{-1}$
k_0	Permeability	m^2
μ	Kinematic viscosity	Pa · s
T	Temperature	°C
t	Time	s
L	Length	m
*	Non-dimensional variable	Dimensionless

2.3. Equilibrium Thermodynamics

To calculate the lookup tables to close our set of equations, we used the Thermolab package of Vrijmoed and Podladchikov (2022). Gibbs energy minimization was used to calculate phase diagrams and postprocess thermodynamic variables. We calculated phase diagrams for 75 different bulk compositions with varying bulk silica and bulk iron contents in the range of 0.1–2.0 GPa and 100–550°C. From these phase diagrams, we postprocessed the values for the thermodynamic closure relationships (ρ_s, ρ_f, c_f, X_h) and expressed them as functions of fluid pressure (P_f), solid composition (c_s) and iron content for a fixed temperature (T). Once the values for P_f and c_s are obtained from Equations 1 and 2, respectively, the closure relationships can be interpolated from the pre-computed equilibrium data. All thermodynamic calculations were performed in the FeO-MgO-SiO_2-H_2O (FMSH) system. The bulk compositions consist of Fe-poor and Fe-rich antigorite to which silica is added to cover a full range of compositions spanning a suitable range of fluid compositions. The initial bulk compositions used in each of the three domains of our model are given in Table 4. In our model, we considered as solid phases antigorite, brucite, olivine, orthopyroxene, talc and quartz, and we consider a SiO_2-H_2O fluid phase. To account for the formation of Fe-Mg solid solutions in minerals and for SiO_2-H_2O mixing in the fluid, we used the solution models given in Table 3.

Table 2
Scaling Used in the Model

Parameter	D_c	L	t	$\frac{k_0}{\mu}$	P_f	ρ
Unit	m^2/s	m	s	$m^2/Pa\ s$	Pa	kg/m^3
Dimensionless parameter	1	1	$\frac{tD_c}{L^2}$	$\frac{k_0 P_f}{\mu D_c}$	1	1

Note. D_c, L, and P_f are chosen as independent variables to scale the dimensionless time t^* and the permeability constant $(k_0/\mu)^*$. All simulations shown in the results section are presented at $t^* = 2.2e7$ and $k_0/\mu = 1$.

Table 3
Solution Models Used for the Phase Diagram Calculations

Phase	Solution model used
Antigorite	Padrón-Navarta et al. (2013)
Olivine	Holland and Powell (1998)
Orthopyroxene	Powell and Holland (1999)
Talc	Holland and Powell (1998)
Brucite	Ideal
Fluid	Ideal mixing with a combination of CORK EOS for H_2O (Holland & Powell, 1991) with aqueous silica neutral species from Holland and Powell (1998)

2.4. The Simplified FMSH System

In our model, we used a more simplified chemical system than that in the model by Plümper et al. (2017) by excluding calcium and aluminum. In serpentinites, calcium would be stored in either diopside (at higher pressures) or tremolite (at lower pressures), but serpentinites have very limited abundances of these phases because they usually have low calcium contents (e.g., bulk compositions of Li et al., 2004), thus supporting our choice to exclude calcium from the model. Regarding aluminum, incorporating aluminum (Tschermak's substitution) in antigorite lowers the temperature of the first antigorite breakdown, as does iron (Padrón-Navarta et al., 2013), and including aluminum also allows one to account for the formation of chlorite, which can retain H_2O in the solid for temperatures up to ~750°C (e.g., Scambelluri et al., 2014). However, because both aluminum and iron have similar effects on the onset of dehydration, and because the goal of this work is to study the effects of silica metasomatism and its first-order effects on serpentinite dehydration after an initial fluid pathway forms due to variations in bulk rock chemistry, we chose to exclude aluminum and only include iron. This allowed us to use the simplest chemical system necessary to describe a heterogeneously dehydrating serpentinite while still being able to examine the effects of a solid solution. Also, including iron only, which has a well-known effect on the onset of dehydration, allowed us to better differentiate between the porosity increase due to the increase in temperature and the porosity increase due to the reactive fluid flow. Furthermore, this simplified chemical system enabled us to use high-resolution lookup tables, as only solid solutions between the magnesium and the iron endmembers needed to be considered.

3. Model Setup

In order to investigate the dynamic effects of reactive fluid flow in a dehydrating serpentinite, we developed a numerical model that combines the findings of Plümper et al. (2017) with the effects of reactive transport by fluids carrying aqueous silica. The model can be used to show how reactive fluid flow on the millimeter to centimeter scale can lead to the formation of almost pure olivine in a matrix that still contains significant amounts of antigorite, as observed in the field (Figure 1).

3.1. Geometry of Model

Observations from the Erro Tobbio meta-serpentinites show that the fluid is heterogeneously distributed in the rock and then pooled into larger veins (Figure 1). To simplify the problem, we set up three chemically distinct domains with varying bulk silica and bulk iron contents, as shown in Figure 6. The three domains represent (a) a matrix with (b) a vein placed in its center and (c) a fluid source region from where fluid flows into the vein. Because we assume that fluid from multiple fluid source regions flows into the vein, the composition of the fluid source region is assigned to one end of the vein in order to simulate a constant fluid influx from a region external but adjacent to our initial vein-wall rock assemblage. We first use 1D setups to separately demonstrate the effects of fluid influx into the vein (Figures 7a–7c) and the fluid-rock interaction between the vein and the wall rock (Figures 7d and 7e) before combining these findings in a 2D model (Figure 8) with a setup as shown in Figure 6.

Table 4
Initial Bulk Compositions in wt. % for the Three Domains Used in the Numerical Model

	SiO_2	MgO	FeO	H_2O
Matrix	42.07	39.78	2.95	15.19
Vein	39.39	37.59	8.38	14.35
Source region	34.68	40.71	9.07	15.54

Note. The vein and the fluid source region have the same FeO content in moles.

3.2. Initial Conditions

Initially, both the matrix and the vein have a higher bulk silica content than the fluid source region, but the vein has a higher bulk iron content than the matrix (see Table 4 for exact compositions). This is based on the findings of Plümper et al. (2017), where iron was the main driver of the intrinsic chemical heterogeneities that resulted in a vein network formation. In the fluid source region at one end of the vein, the silica content is lower than in the vein, resulting in a high iron and a low silica content in this domain (see Figure 6). All three domains have initially zero background porosity ($\phi^0 = 0$) and a homogeneous fluid pressure ($P_f^0 = 1.0$ GPa, equal to ambient pressure) at an initial temperature (T_0) of 440°C. To simulate dehydration during subduction, the temperature is instantaneously increased to 480°C (T_1) to cross the 450°C boundary at which the fluid composition of high- and low-silica systems start to vary significantly (Figure 3). The temperature increase leads to dehydration in all domains, but the extent of dehydration and the composition of the liberated fluid is different in every domain because both depend on the bulk composition, as in Plümper et al. (2017). Starting from a homogeneous zero background porosity and homogeneous fluid pressure, the temperature increase leads to the formation of porosity and to changes in the fluid pressure to different extents in every domain, depending on each domain's initial bulk composition. All simulations were run for a total dimensionless time of $t^* = 2.2e7$ and used a dimensional permeability constant $k_0/\mu = 1$.

3.3. Boundary Conditions

In our model, we use Neumann (zero flux) boundary conditions at all boundaries, which allows the boundary nodes to be updated after the temperature increase. In the 2D model (Figure 8), the composition of the fluid source region is kept constant at the lower end of the vein after the temperature increase; thus, this end of the vein acts as a constant fluid source, assuming that the fluid is pooled from a larger reservoir (the fluid source region) that is connected to one end of the vein (Figure 6).

4. Results

4.1. Effects of Chemical Heterogeneities on the Onset of Dehydration

The local bulk composition controls the stability and abundance of hydrous minerals and, thus, the onset of dehydration (e.g., Plümper et al., 2017). Iron is one of the components with a strong influence on the temperature at which the first dehydration reaction occurs (e.g., Merkulova et al., 2016; Spear, 1993); a high iron content decreases the temperature of the first dehydration reaction by stabilizing brucite and iron-rich antigorite at lower temperatures. This effect can be seen in Figure 2, which shows isochemical phase diagram P-T sections for two serpentinite bulk compositions that are varied only in their iron content. In the iron-rich system (Figure 2a) the onset of dehydration, shown by the reaction line labeled "free fluid in," is 100°C lower than the iron-poor system (Figure 2b).

However, because of its very low solubility at deep subduction zone conditions, iron has only a minor effect on the composition of the liberated fluid (Charlou et al., 2002; Ding & Seyfried, 1992; Manning, 2004). Silica, on the other hand, is abundant in serpentinites and has a significantly higher solubility (Manning, 2004). Therefore, to study first-order mechanisms of reactive transport in serpentinites, we investigated the effect of silica as the metasomatic agent in our model.

If silica can either be stored in the solid or dissolved in the fluid phase, the equilibrium composition of both phases depends on the bulk composition of the entire system and especially on the total silica abundance. To study how varying the bulk silica contents affects a dehydrating serpentinite, we calculated isochemical phase diagram P-T sections for two serpentinite bulk compositions with identical bulk iron but varying bulk silica contents. Figure 3 shows the effect of bulk silica variations on dehydration with increasing P-T conditions. The left and right columns show the results for the low-silica and the high-silica systems, respectively. The range of P-T conditions captures the dehydration reaction of antigorite and brucite to form olivine and a free fluid. In the low-silica system, dehydration starts at lower temperatures than in the high-silica system (Figures 3a and 3b). Consequently, nearly 90 vol. % olivine forms in the system with lower bulk SiO_2, whereas in the

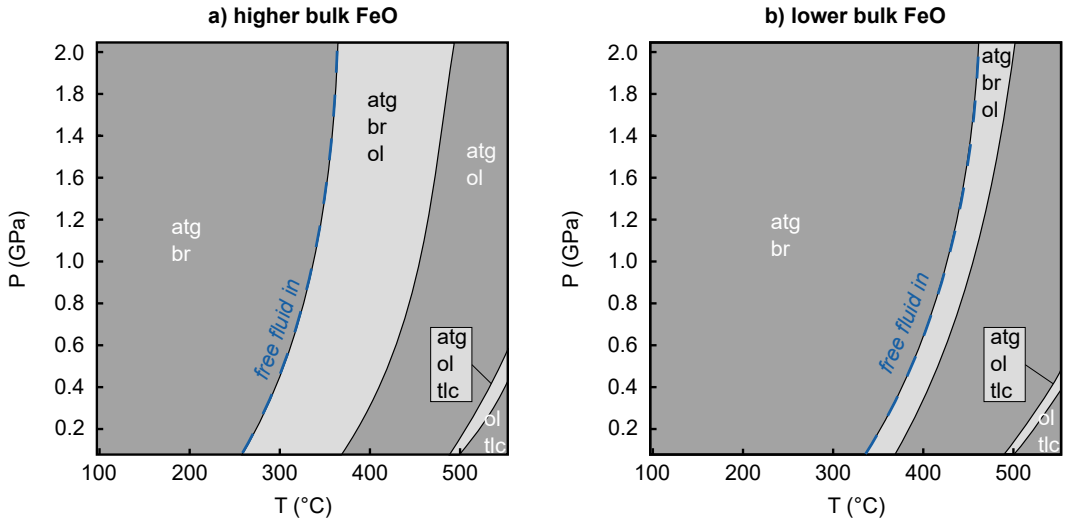

Figure 2. Phase diagram P-T sections for two typical serpentinite bulk compositions with identical silica and varying iron contents. A higher iron content (a) lowers the temperature for the onset of dehydration (marked by the blue dashed "free fluid in" reaction line) by ca. 100°C compared to the iron-poor composition (b). atg, antigorite; br, brucite; ol, olivine; tlc, talc. Different gray shadings represent varying degrees of freedom with respect to the Gibbs phase rule.

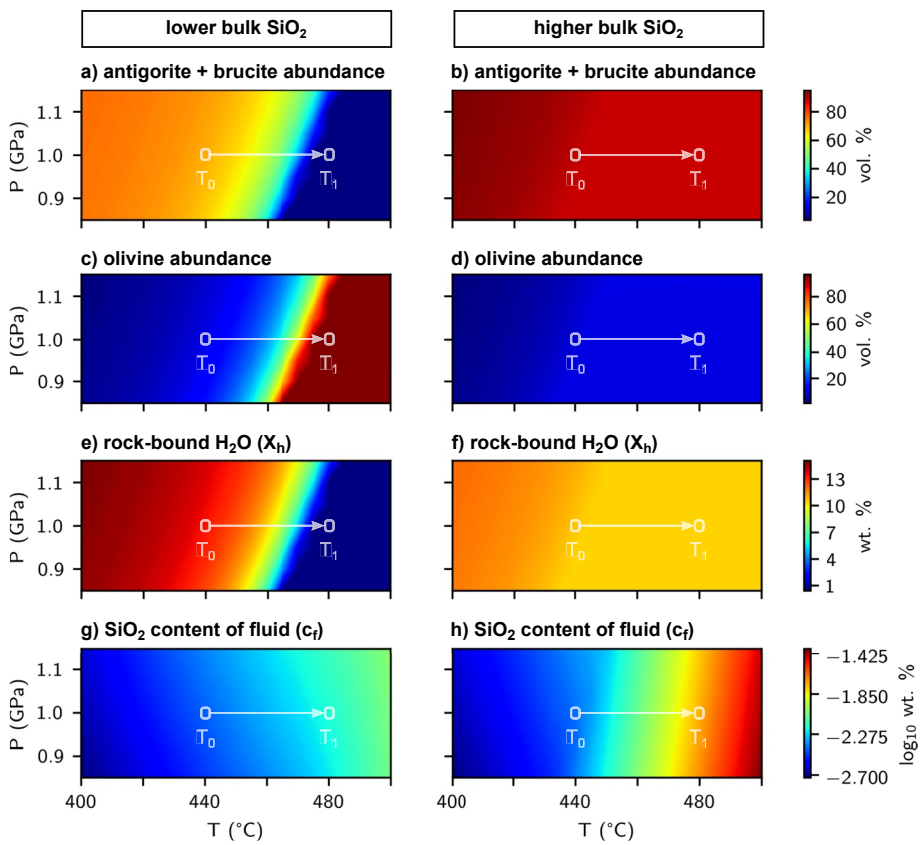

Figure 3. Effects of varying bulk silica contents in a system with a high bulk iron content. A low bulk silica content stabilizes more brucite which is only stable up to around 470°C (a and b) and reacts with antigorite to form olivine (c and d). The sharp decrease in the brucite content in the low silica system between 450 and 475°C leads to a stronger overall decrease in the amount of solid-bound H_2O in the low silica system (e and f) and thus to the liberation of more fluid. The fluid released from the low-silica system has a lower silica content compared to the fluid liberated from the high-silica system (g and h). The bulk composition of the low-silica system is used as source region in the numerical model (see Figure 6). The arrow connecting the white circles shows the temperature step in the numerical model from 440°C (T_0) to 480°C (T_1) at 1 GPa.

system with higher bulk SiO_2, the olivine abundance increases only slightly (Figures 3c and 3d). The reason for this is that a low silica content stabilizes more brucite, which is only stable up to temperatures of 450 and 475°C in the low- and high-silica systems, respectively. As brucite contains large amounts of H_2O, the strong decrease in the brucite content also leads to a stronger decrease in the overall H_2O content of the solid (Figures 3e and 3f) and, thus, to the liberation of more fluid in the silica-poor system. The composition of the liberated fluid (Figures 3g and 3h) is very similar with respect to silica up to temperatures of around 450°C. For higher temperatures, the fluid released from the low-silica system also contains less dissolved silica than the fluid from the high-silica system. Thus, a lower bulk silica content leads to (a) a larger amount of liberated fluid during dehydration and (b) the generation of a low-silica fluid at temperatures above ~450°C.

These calculations show that a low silica content stabilizes higher brucite abundances at temperatures below ~475°C. For higher temperatures, brucite breaks down, and a fluid forms that is poorer in silica compared to the fluid released from more antigorite-rich domains, that is, the silica-poorer domains dehydrate more strongly than the silica-richer domains in this temperature range. The resulting local fluid overpressure then drives fluid flow of the silica-poor fluid into other areas of the porous network.

4.2. Shifting Thermodynamic Equilibrium Towards Olivine Enrichment

Therefore, silica gets transported along with the fluid, and the resulting changes in the fluid composition affect the bulk silica content of the surrounding solid because the bulk silica content re-equilibrates with the changing fluid composition. This means that the bulk silica content of a system, as in Figure 3, can take on higher or lower values due to transport of aqueous silica in the fluid. The effects of such a shift in the bulk silica content are illustrated in Figure 4: This figure shows the equilibrium relationships between the silica content of the fluid (c_f) and the solid (c_s) and the resulting stable mineral assemblage in the rock for a system with a higher bulk iron content (Figure 4a) and for a system with a lower bulk iron content (Figure 4b). In both systems, lowering the fluid silica content leads to a decrease in the bulk silica content. This decrease in the bulk silica content causes dehydration by antigorite breakdown and olivine formation.

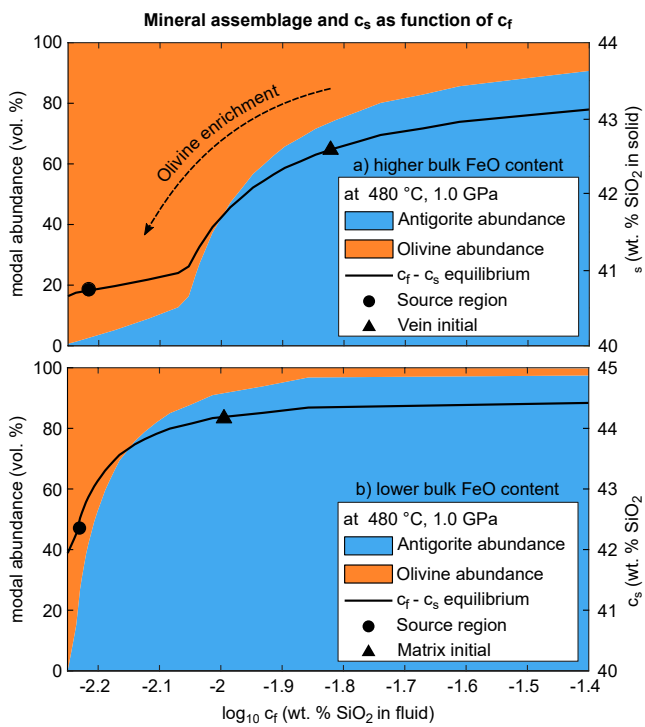

Figure 4. Equilibrium silica contents of fluid (c_f) and solid (c_s) in a system with a higher (a) and a lower (b) bulk iron content at a fixed temperature of 480°C (T_1) and a pressure of 1.0 GPa (P_f^0). The solid black line represents the thermodynamic equilibrium between fluid and solid for varying bulk silica contents. The colored areas show the stable mineral assemblage in the rock for every value of c_s (blue = antigorite, orange = olivine). The filled circles are plotted at the bulk composition of the fluid source region, the triangles at the initial bulk composition of the vein (a) and the matrix (b). Lowering the fluid composition in the vein and matrix shifts the solid composition along the black curve toward the left, resulting in dehydration by antigorite breakdown and olivine enrichment, reaching an almost pure olivine assemblage in the system with a higher bulk iron content (a).

The results in Figure 4 are shown for a constant pressure, but in our model we also consider effects of changes in the fluid pressure, as both c_s and P_f are used for interpolation in the lookup tables. The equilibrium relationships between c_s, c_f, P_f and the olivine abundance in the rock are shown in Figure 5. Figures 5a and 5c show the fluid composition as a function of fluid pressure and the bulk silica content of the solid. The abundance of olivine in the associated mineral assemblage is shown in Figures 5b and 5d. In both the low and the high bulk iron systems, there is a sharp, nearly pressure-independent drop in the equilibrium fluid composition at a c_s value of around 44 wt. % SiO_2 in the low-iron system and 43 wt. % SiO_2 in the high-iron system. The olivine abundance plots show that for pressures below ~1.0 GPa (Figure 5b) and 1.5 GPa (Figure 5d), this change in the fluid composition is accompanied by the onset of olivine occurrence in the solid. For c_s values of 41.5 wt. % SiO_2 (Figure 5b) and 40.5 wt. % SiO_2 (Figure 5d), the olivine abundance reaches almost 100 vol. %, as shown by the black boxes. For even lower c_s values the olivine abundance decreases again due to the formation of brucite, and for pressures above ~1 GPa olivine reacts to form antigorite.

Figure 5 shows how changes in fluid pressure and the fluid composition can shift the thermodynamic equilibrium toward olivine formation and even "olivine purification" of the system due to an increase of olivine abundance at constant temperature. The shift occurs along a c_s-P-path that is controlled by the solutions of Equations 1–3, that is, by local thermodynamic equilibrium. The figure also demonstrates that to reach "olivine purification" of the

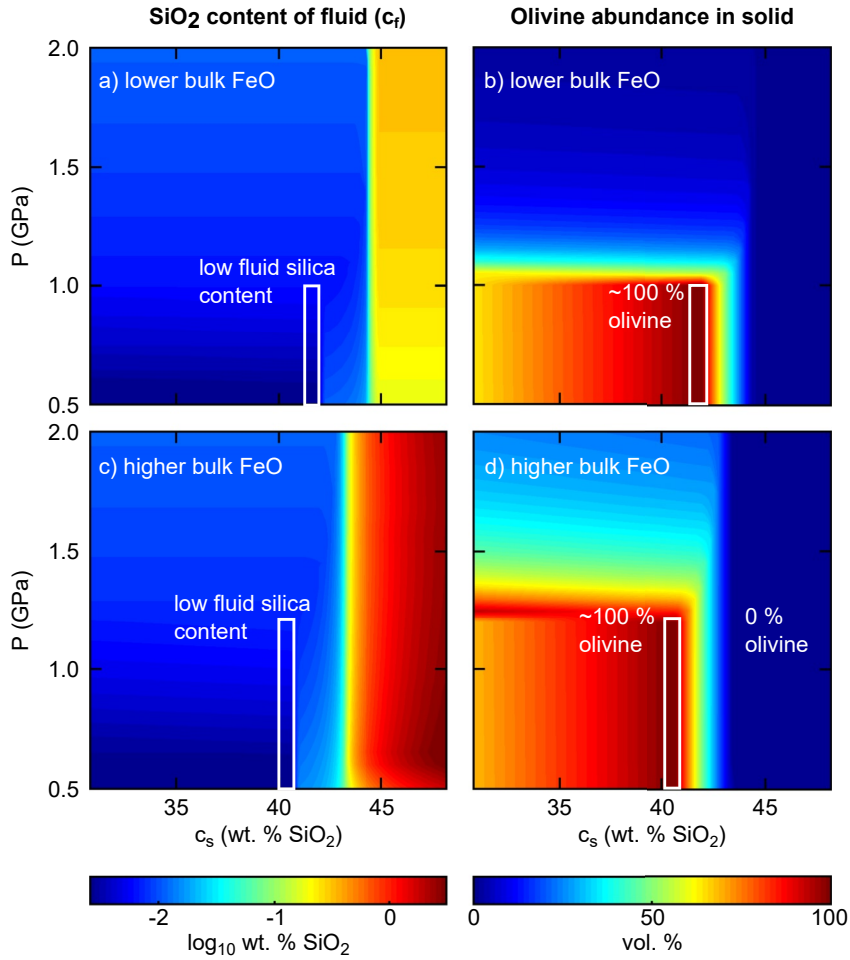

Figure 5. Composition and olivine abundance in the solid as functions of bulk silica content (c_s) and pressure (P) at a constant temperature of 480°C for two systems with varying bulk iron contents. Panels a) and b) show fluid silica content and olivine abundance in the solid in a system with lower bulk iron content, respectively. Panels c) and d) show fluid silica content and olivine abundance in the solid in a system with higher bulk iron content. Black boxes highlight a range of c_s-P values where the solid consists of almost pure olivine. Changes in fluid pressure and fluid composition can shift the equilibrium toward values within the black boxes and thus to olivine purification at constant temperature.

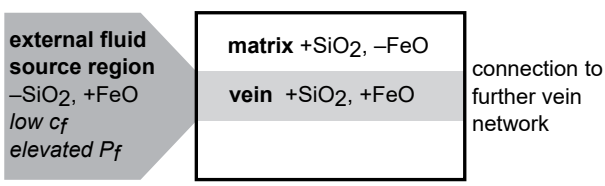

Figure 6. Conceptual sketch of the 2D model setup. A high silica domain with iron heterogeneities (black rectangle) is connected to a fluid source region (dark gray), where enhanced dehydration results in fluid pressure increase and the liberation of a low-silica fluid which flows into the vein. The composition of the fluid source region (Table 4) is assigned at one end of the vein and kept constant after the temperature increase, thus acting as constant source of a low-silica fluid. Both fluid pressure and fluid composition are defined by thermodynamic equilibrium with the surrounding solid and depend on the local bulk composition. The bulk composition of each domain in the model is listed in Table 4. Zero flux (Neumann) boundary conditions are used at all boundaries in the model. The 1D setups (Figure 7) represent profiles parallel (Figures 7a–7c) and perpendicular (Figures 7d and 7e) to the vein.

vein, the silica content of the fluid must be low (<0.01 wt. % SiO_2) and the fluid pressure must be below ~1 GPa.

4.3. Porosity and Fluid Pressure

The temperature increase leads to changes in fluid pressure and to the formation of porosity via dehydration-causing mineral reactions in the initially non-porous rock ($\phi^0 = 0$). Figures 7a and 7d show the fluid pressure (blue lines) and porosity (orange lines) after a non-dimensional time of $t^* = 2.2e7$ for the case where fluid flows from the fluid source region into the vein and perpendicular to the vein, that is, the fluid-rock interaction between fluid and the vein and the matrix. Dehydration and, thus, porosity increase after the temperature increase is highest in the fluid source region ($\phi \sim 0.25$), followed by the vein ($\phi \sim 0.05$) and the matrix ($\phi \sim 0.03$). The fluid pressure increases in parts of the domain that show stronger dehydration and drives fluid flow from the fluid source region into the vein and from the vein into the matrix. Subsequent to the temperature increase, porosity then increases further by dehydration-related mineral reactions that are induced by the reactive fluid flow (orange areas in

Figures 7a and 7d). These calculated porosities reflect realistic values for subducted oceanic lithosphere at comparable P-T conditions (Katayama et al., 2012; Taetz et al., 2016).

4.4. Olivine Enrichment and Antigorite Breakdown

Olivine enrichment by reactive fluid flow-induced antigorite breakdown can be seen in Figures 7c and 7f. In the fluid source region, the olivine content after the temperature increase reaches almost 100 vol. % compared to ~42 vol. % in the vein and ~10 vol. % in the matrix. The almost olivine-pure mineral assemblage in the fluid source region is in equilibrium with a fluid that contains the lowest amount of silica of all three domains. The influx of this low-silica fluid into the vein (Figure 7b) leads to antigorite breakdown and olivine enrichment in the vein. Within the vein, the equilibrium is shifted toward the almost olivine-pure mineral assemblage (Figure 7c) because the fluid source region and the vein only vary in their initial bulk silica content but have the same bulk iron

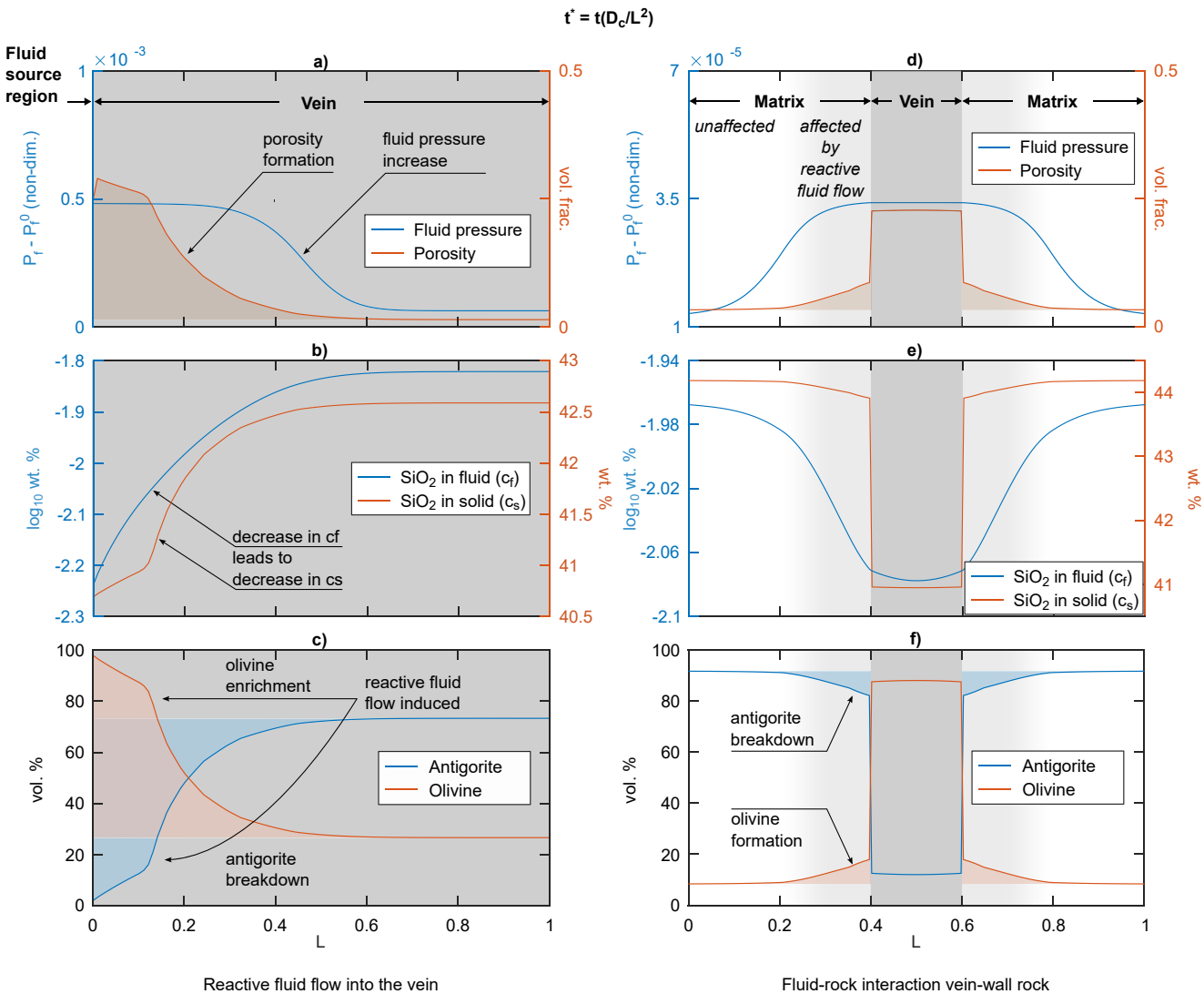

Figure 7. Results of the numerical model in a 1D domain with non-dimensional length *L*. Panels (a–c): reactive fluid flow from the source region into the vein; (d–f): fluid-rock interaction between the vein and the wall rock. (a) Fluid flow from the source region (left boundary) into the vein (gray) leads to fluid pressure increase (blue graph) and porosity increase (orange graph). (b) The decrease in the silica content of the fluid (blue graph) and changes in the fluid pressure cause a decrease in the bulk silica content of the solid (orange graph). (c) Modal abundances of olivine and antigorite show olivine enrichment in the vein. (d) Porosity also forms in the wall rock at the vein boundary (orange graph). (e) Diffusion of aqueous silica from the matrix into the vein leads to dehydration at the vein wall (f). Olivine formation in the matrix however is limited because the low iron content of the matrix stabilizes antigorite (Figure 4b). The non-dimensional time for these results is $t^* = 2.2e7$. If $L = 1$ cm, the diffusion length (width of the matrix affected by reactive fluid flow) would be 0.4 cm. Using the equation of Watson and Wark (1997) to calculate the diffusivity of aqueous silica at 1 GPa and 480°C gives a real time of t ~1600 years.

content. Fluid flow between an olivine-rich vein and the surrounding host rock (matrix) leads to dehydration at the vein margins and to re-hydration within the vein if no constant influx of a low-silica fluid occurs (Figures 7e and 7f). In the matrix, the lower bulk iron content stabilizes antigorite and limits olivine formation to max. ~20 vol. % even though c_s in the matrix is also lowered by reactive fluid flow.

4.5. 2D Model

The 2D model includes the vein, the matrix and the fluid source region arranged in one domain as shown in Figure 6. As in the 1D model, the initial porosity is zero everywhere at a homogeneous fluid pressure of 1.0 GPa and a temperature of 440°C. After the temperature increase, the elevated fluid pressure in the source region

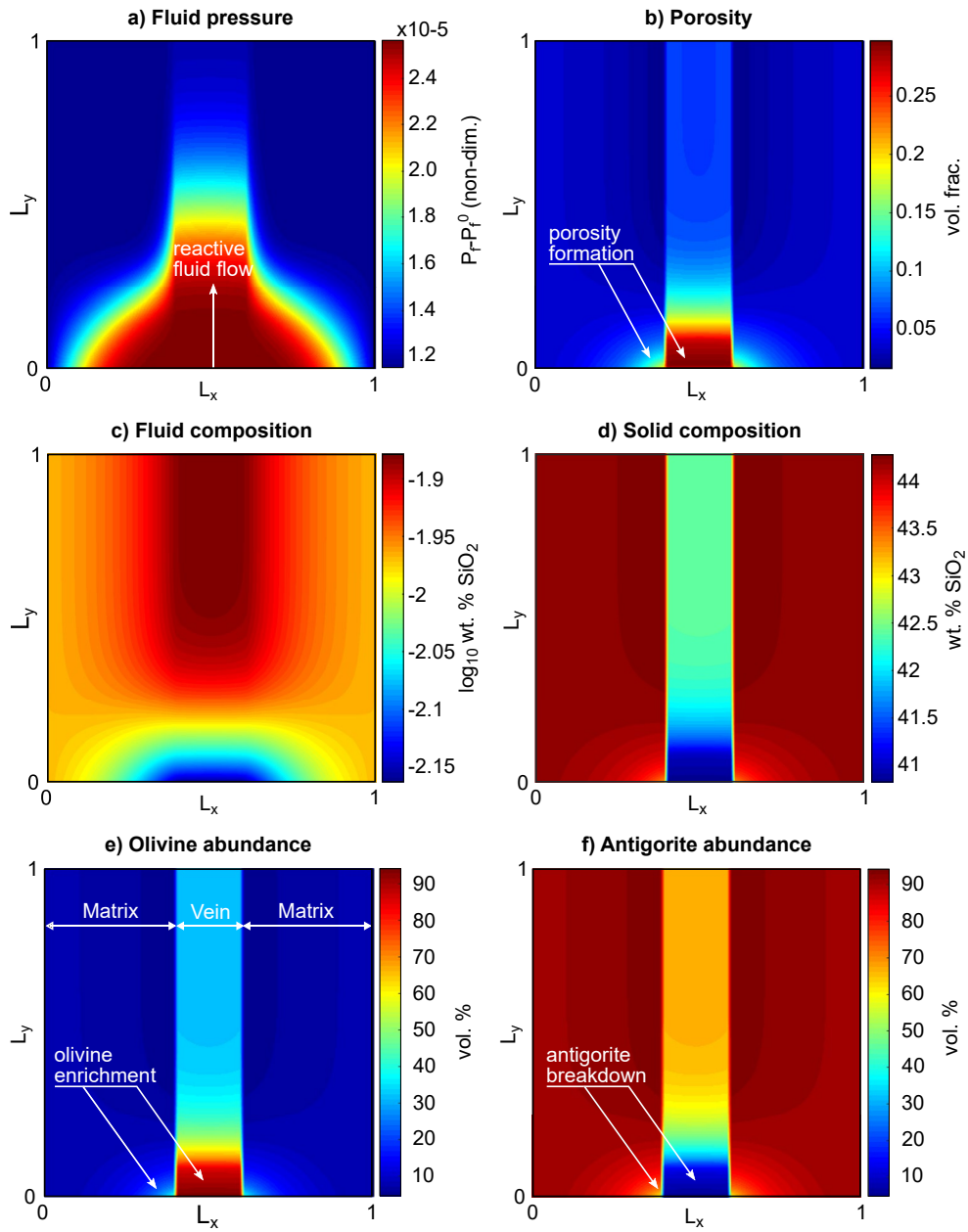

Figure 8. Results of the numerical model in a 2D domain with a setup as shown in Figure 6. Panel (a) non-dimensional fluid overpressure, (b) porosity (ϕ), (c) fluid composition (c_f), (d) solid composition (c_s), (e) olivine abundance, and (f) antigorite abundance after $t^* \sim 2.1e7$. Fluid influx from the fluid source region results in olivine formation by antigorite breakdown in the vein and the adjacent wall rock at constant temperature. The initial bulk compositions of the vein, the matrix and the source regions are identical to the ones used for the 1D model (Figure 7 and Table 4). The composition of the fluid source region is set as boundary condition at the lower end of the vein.

(Figure 8a) drives fluid flow into the vein and the vein-surrounding matrix. The increased porosity in the vein (Figure 8b) channelizes the fluid flow into the vein. As demonstrated in the 1D model, minor dehydration and olivine formation at the expense of antigorite also occurs at the slightly widening vein margins (Figures 8e and 8f). After the temperature increase, c_f is higher within the vein than in the matrix (Figure 8c). Diffusion of silica from the vein into the matrix also lowers the silica content of the fluid in the vein prior to the influx of the low-silica fluid from the fluid source region. This interaction between the vein and the matrix increases porosity in the vein from $\phi \sim 0.05$ after the temperature increase to $\phi \sim 0.1$ when the low-silica fluid from the source region affects the vein. The higher porosity in the vein after the temperature increase and the strong porosity increase due to reactive fluid flow channelize the fluid flow into the vein.

5. Discussion

5.1. The Fluid Source Regions

In the numerical model, the composition of the fluid source region has been assigned at one end of the vein, which leads to a constant fluid influx into the vein. This source region does not necessarily represent a single spot in the rock but rather multiple volumes of rock that dehydrate and release a low-silica fluid. We hypothesize that when the porosity and, hence, permeability in the porous media-like rock system is high enough, that is, the percolation threshold is reached (e.g., Bloch et al., 2018), the fluid from these domains will continue channelizing (e.g., Plümper et al., 2017) into larger veins, such as the one in our model. The low silica content and high iron content of the source regions stabilize a significant amount of brucite at lower temperatures. In a natural serpentinite, the source regions would therefore be brucite-rich domains that are distributed in the mantle section of interest. In fact, Klein et al. (2020) and Kempf et al. (2020) used the distribution of olivine-rich patches in the Zermatt ophiolite to infer to former brucite-rich spots. They also related the olivine-rich shear zones in the ophiolite to the pathways of the fluid released from the brucite-rich spots. Therefore, the initial composition chosen for the fluid source region in our model reflects those brucite-rich and silica-poor domains in natural systems (Li et al., 2004).

5.2. The Instantaneous Increase in Temperature

As no large temperature gradients are expected on the micro scale, we applied a spatially homogeneous temperature throughout all domains. The instantaneous temperature increase in our model simulates the effect of subduction deeper down into the subduction zone, namely the descent into the hot mantle. In nature, this temperature increase certainly happens continuously. Smaller temperature steps would lead to a more continuous approximation of the dehydration process and a competition between the relaxation of the fluid pressure and the fluid chemistry gradients. Here, our focus was on the process of fluid pressure relaxation and fluid composition evolution after a single step of heating, which allowed us to study only the transient effects of reactive fluid flow in more detail. In order to simulate a more complete subduction zone dehydration process, a more complex approach involving heat transport is needed. We chose the temperature range from 440 to 480°C at which the reactive fluid flow most likely becomes important. Our calculations (Figures 3g and 3h) show that until a temperature of about 460°C, the silica content of fluids derived from the high- and the low-silica domains are quite similar; only at higher temperatures is more silica dissolved in the fluid of the high-silica system than in the low-silica system, and reactive fluid flow will be more effective.

5.3. Fe Dissolution in the Fluid

Although the dissolution of ferrous iron in aqueous fluids is very low (e.g., Charlou et al., 2002; Ding & Seyfried, 1992), Debret et al. (2016) showed isotopic evidence for long-distance iron transport via subduction zone fluids. In a reduced serpentinite as used in our model, ferrous iron is mostly transported by forming sulfur and chlorine complexes (Chen et al., 2019). The amount of dissolved iron, therefore, also depends on the abundance of these elements in the serpentinite (Alt et al., 2013). A high concentration of iron in solution would also lead to iron exchange between the solid and the fluid and, thus, affect the iron content of the solid. Because the iron content has a large effect on dehydration reactions, the transport of iron in the fluid could amplify the effects of reactive fluid flow beyond the effects due to transport of aqueous silica.

5.4. Implications for Fluid Release in Subduction Zones

Various studies have shown that intra-slab fluid flow and fluid escape from the slab is channelized and reactive, both to various degrees (e.g., Angiboust et al., 2014; Chen et al., 2019; Herms et al., 2012; John et al., 2012; Taetz et al., 2016). Our findings indicate that reactive fluid flow is able to transform an initially fine and small-scale, high-porosity structure into a wider and larger vein system that could also develop reaction halos. Thus, our findings reflect a first step toward a mechanistic understanding of how dehydration leads from the first stage of chemistry-controlled local dehydration to the development of intra-slab flow structures that are either highly channelized with only limited interaction with the wall rock (e.g., Breeding & Ague, 2002; Spandler et al., 2011) or highly channelized with significant reaction halos surrounding the vein (e.g., Herms et al., 2012; John et al., 2012; Taetz et al., 2016); further, some structures might even be porosity wave-like high-permeability structures that affect rock volumes on the scale of centimeters to tens of meters without necessarily having fracture-like vein structures (e.g., Chen et al., 2019; Piccoli et al., 2021).

6. Conclusions

Here, we have presented a reactive fluid flow model for the transport of aqueous silica in a dehydrating serpentinite. In our model, porosity is generated dynamically with dehydration, demonstrating how an initial non-porous rock can evolve into a channelized fluid flow system. We show how changes in the bulk silica and the bulk iron content affect the dehydration reaction of antigorite + brucite = olivine + fluid and affect the composition of this fluid with respect to silica. Domains with higher bulk iron and lower bulk silica contents dehydrate more strongly and earlier than domains with higher bulk silica and lower bulk iron contents. The fluid released from these early dehydrating domains contains low amounts of aqueous silica, and the elevated fluid pressure in the more strongly dehydrated domains will drive fluid flow of this low-silica fluid into domains with higher silica contents, where changes in the fluid composition cause dehydration and widening of existing veins by induced antigorite breakdown and olivine formation. In iron-richer domains, the mineral assemblage can be shifted toward olivine purification, whereas in iron-poorer areas substantial amounts of antigorite remain stable. This is in accordance with observations of olivine-rich veins in an antigorite-rich country rock, such as in the Erro-Tobbio meta-serpentinites.

Data Availability Statement

A 1D and a 2D version of the reactive transport code as well as the codes used to create the thermodynamic lookup tables used in this study are available at Zenodo via https://doi.org/10.5281/zenodo.6569809 with CC-BY 4.0.

Acknowledgments
The Deutsche Forschungsgemeinschaft financially supported this research through grant CRC 1114 "Scaling Cascades in Complex Systems," Project Number 235221301, Project (C09) – "Dynamics of rock dehydration on multiple scales." The authors also thank the members of the C09 project from the Weierstraß Institut (WIAS) in Berlin, M. Thomas, D. Peschka and A. Zafferi for their collaboration in this project and the fruitful discussions. The authors also thank M. Scambelluri for his collaboration and for helping us in the field and two anonymous reviewers who considerably helped to improve this paper. Open Access funding enabled and organized by Projekt DEAL.

References

Alt, J. C., Schwarzenbach, E. M., Früh-Green, G. L., Shanks, W. C., Bernasconi, S. M., Garrido, C. J., et al. (2013). The role of serpentinites in cycling of carbon and sulfur: Seafloor serpentinization and subduction metamorphism. *Lithos*, *178*, 40–54. https://doi.org/10.1016/j.lithos.2012.12.006

Angiboust, S., Pettke, T., De Hoog, J. C. M., Caron, B., & Oncken, O. (2014). Channelized fluid flow and eclogite-facies metasomatism along the subduction shear zone. *Journal of Petrology*, *55*(5), 883–916. https://doi.org/10.1093/petrology/egu010

Beinlich, A., John, T., Vrijmoed, J. C., Tominaga, M., Magna, T., & Podladchikov, Y. Y. (2020). Instantaneous rock transformations in the deep crust driven by reactive fluid flow. *Nature Geoscience*, *13*(4), 307–311. https://doi.org/10.1038/s41561-020-0554-9

Bloch, W., John, T., Kummerow, J., Salazar, P., Krüger, O. S., & Shapiro, S. A. (2018). Watching dehydration: Seismic indication for transient fluid pathways in the oceanic mantle of the subducting Nazca slab. *Geochemistry, Geophysics, Geosystems*, *19*(9), 3189–3207. https://doi.org/10.1029/2018GC007703

Breeding, C. M., & Ague, J. J. (2002). Slab-derived fluids and quartz-vein formation in an accretionary prism, Otago Schist, New Zealand. *Geology*, *30*(6), 499–502. https://doi.org/10.1130/0091-7613(2002)030<0499:SDFAQV>2.0.CO;2

Cerpa, N. G., Wada, I., & Wilson, C. R. (2017). Fluid migration in the mantle wedge: Influence of mineral grain size and mantle compaction. *Journal of Geophysical Research: Solid Earth*, *122*(8), 6247–6268. https://doi.org/10.1002/2017JB014046

Charlou, J. L., Donval, J. P., Fouquet, Y., Jean-Baptiste, P., & Holm, N. (2002). Geochemistry of high H_2 and CH_4 vent fluids issuing from ultramafic rocks at the Rainbow hydrothermal field (36°14′N, MAR). *Chemical Geology*, *191*(4), 345–359. https://doi.org/10.1016/S0009-2541(02)00134-1

Chen, S., Hin, R. C., John, T., Brooker, R., Bryan, B., Niu, Y., & Elliott, T. (2019). Molybdenum systematics of subducted crust record reactive fluid flow from underlying slab serpentine dehydration. *Nature Communications*, *10*(1), 4773. https://doi.org/10.1038/s41467-019-12696-3

Clément, M., Padrón-Navarta, J. A., & Tommasi, A. (2020). Interplay between fluid extraction mechanisms and antigorite dehydration reactions (Val Malenco, Italian Alps). *Journal of Petrology*, *60*(10), 1935–1962. https://doi.org/10.1093/petrology/egz058

Connolly, J. A. D. (1997). Devolatilization-generated fluid pressure and deformation-propagated fluid flow during prograde regional metamorphism. *Journal of Geophysical Research*, *102*(B8), 18149–18173. https://doi.org/10.1029/97jb00731

Connolly, J. A. D., & Podladchikov, Y. Y. (2007). Decompaction weakening and channeling instability in ductile porous media: Implications for asthenospheric melt segregation. *Journal of Geophysical Research*, *112*(B10), B10205. https://doi.org/10.1029/2005jb004213

Debret, B., Millet, M.-A., Pons, M.-L., Bouilhol, P., Inglis, E., & Williams, H. (2016). Isotopic evidence for iron mobility during subduction. *Geology*, *44*(3), 215–218. https://doi.org/10.1130/G37565.1

Ding, K., & Seyfried, W. E. (1992). Determination of Fe-Cl complexing in the low pressure supercritical region (NaCl fluid): Iron solubility constraints on pH of subseafloor hydrothermal fluids. *Geochimica et Cosmochimica Acta*, *56*(10), 3681–3692. https://doi.org/10.1016/0016-7037(92)90161-B

Fukumura, S., Okamoto, K., & Terabayashi, M. (2019). Metamorphic olivine after dehydration embrittlement in Serpentinite: Case study from the Shiraga Serpentinite mass in the Sanbagawa high P/T metamorphic belt, central Shikoku, Japan. *Island Arc*, *28*(2), e12293. https://doi.org/10.1111/iar.12293

Groppo, C., & Compagnoni, R. (2007). Metamorphic veins from the serpentinites of the Pieomonte Zone western Alps: A review. *Periodico di Mineralogia*, *76*(2–3), 127–153. https://doi.org/10.2451/2007PM0021

Hacker, B. R., Peacock, S. M., Abers, G. A., & Holloway, S. D. (2003). Subduction factory 2. Are intermediate-depth earthquakes in subducting slabs linked to metamorphic dehydration reactions? *Journal of Geophysical Research*, *108*(B1), 2030. https://doi.org/10.1029/2001JB001129

Hermann, J., Müntener, O., & Scambelluri, M. (2000). The importance of serpentinite mylonites for subduction and exhumation of oceanic crust. *Tectonophysics*, *327*(3), 225–238. https://doi.org/10.1016/S0040-1951(00)00171-2

Herms, P., John, T., Bakker, R. J., & Schenk, V. (2012). Evidence for channelized external fluid flow and element transfer in subducting slabs (Raspas Complex, Ecuador). *Chemical Geology*, *310–311*, 79–96. https://doi.org/10.1016/j.chemgeo.2012.03.023

Hesse, M. A., Schiemenz, A. R., Liang, Y., & Parmentier, E. M. (2011). Compaction-dissolution waves in an upwelling mantle column. *Geophysical Journal International*, *187*(3), 1057–1075. https://doi.org/10.1111/j.1365-246x.2011.05177.x

Holland, T., & Powell, R. (1991). A Compensated-Redlich-Kwong (CORK) equation for volumes and fugacities of CO_2 and H_2O in the range 1 bar to 50 kbar and 100–1600°C. *Contributions to Mineralogy and Petrology*, *109*(2), 265–273. https://doi.org/10.1007/BF00306484

Holland, T., & Powell, R. (1998). An internally consistent thermodynamic data set for phases of petrological interest. *Journal of Metamorphic Geology*, *16*(3), 309–343. https://doi.org/10.1111/j.1525-1314.1998.00140.x

John, T., Gussone, N., Podladchikov, Y. Y., Bebout, G. E., Dohmen, R., Halama, R., et al. (2012). Volcanic arcs fed by rapid pulsed fluid flow through subducting slabs. *Nature Geoscience*, *5*(7), 489–492. https://doi.org/10.1038/ngeo1482

John, T., Klemd, R., Gao, J., & Garbe-Schönberg, C.-D. (2008). Trace-element mobilization in slabs due to non steady-state fluid–rock interaction: Constraints from an eclogite-facies transport vein in blueschist (Tianshan, China). *Lithos*, *103*(1), 1–24. https://doi.org/10.1016/j.lithos.2007.09.005

Jung, H., Green, H. W., II, & Dobrzhinetskaya, L. F. (2004). Intermediate-depth earthquake faulting by dehydration embrittlement with negative volume change. *Nature*, *428*(6982), 545–549. https://doi.org/10.1038/nature02412

Katayama, I., Terada, T., Okazaki, K., & Tanikawa, W. (2012). Episodic tremor and slow slip potentially linked to permeability contrasts at the Moho. *Nature Geoscience*, *5*(10), 731–734. https://doi.org/10.1038/ngeo1559

Kempf, E. D., Hermann, J., Reusser, E., Baumgartner, L. P., & Lanari, P. (2020). The role of the antigorite + brucite to olivine reaction in subducted serpentinites (Zermatt, Switzerland). *Swiss Journal of Geosciences*, *113*(1), 16. https://doi.org/10.1186/s00015-020-00368-0

Klein, F., Humphris, S. E., & Bach, W. (2020). Brucite formation and dissolution in oceanic serpentinite. *Geochemical Perspectives Letters*, 1–5. https://doi.org/10.7185/geochemlet.2035

Li, X.-P., Rahn, M., & Bucher, K. (2004). Serpentinites of the Zermatt-Saas ophiolite complex and their texture evolution. *Journal of Metamorphic Geology*, *22*(3), 159–177. https://doi.org/10.1111/j.1525-1314.2004.00503.x

López Sánchez-Vizcaíno, V., Gómez-Pugnaire, M. T., Garrido, C. J., Padrón-Navarta, J. A., & Mellini, M. (2009). Breakdown mechanisms of titanclinohumite in antigorite serpentinite (Cerro del Almirez massif, S. Spain): A petrological and TEM study. *Lithos*, *107*(3), 216–226. https://doi.org/10.1016/j.lithos.2008.10.008

López Sánchez-Vizcaíno, V., Trommsdorff, V., Gómez-Pugnaire, M. T., Garrido, C. J., Müntener, O., & Connolly, J. A. D. (2005). Petrology of titanian clinohumite and olivine at the high-pressure breakdown of antigorite serpentinite to chlorite harzburgite (Almirez Massif, S. Spain). *Contributions to Mineralogy and Petrology*, *149*(6), 627–646. https://doi.org/10.1007/s00410-005-0678-3

Magott, R., Fabbri, O., & Fournier, M. (2020). Seismically-induced serpentine dehydration as a possible mechanism of water release in subduction zones. Insights from the Alpine Corsica pseudotachylyte-bearing Monte Maggiore ophiolitic unit. *Lithos*, *362–363*, 105474. https://doi.org/10.1016/j.lithos.2020.105474

Malvoisin, B., Podladchikov, Y. Y., & Vrijmoed, J. C. (2015). Coupling changes in densities and porosity to fluid pressure variations in reactive porous fluid flow: Local thermodynamic equilibrium. *Geochemistry, Geophysics, Geosystems*, *16*(12), 4362–4387. https://doi.org/10.1002/2015GC006019

Manning, C. E. (2004). The chemistry of subduction-zone fluids. *Earth and Planetary Science Letters*, *223*(1), 1–16. https://doi.org/10.1016/j.epsl.2004.04.030

Mazza, S. E., Stracke, A., Gill, J. B., Kimura, J.-I., & Kleine, T. (2020). Tracing dehydration and melting of the subducted slab with tungsten isotopes in arc lavas. *Earth and Planetary Science Letters*, *530*, 115942. https://doi.org/10.1016/j.epsl.2019.115942

McGary, R. S., Evans, R. L., Wannamaker, P. E., Elsenbeck, J., & Rondenay, S. (2014). Pathway from subducting slab to surface for melt and fluids beneath Mount Rainier. *Nature*, *511*(7509), 338–340. https://doi.org/10.1038/nature13493

Merkulova, M., Muñoz, M., Vidal, O., & Brunet, F. (2016). Role of iron content on serpentinite dehydration depth in subduction zones: Experiments and thermodynamic modeling. *Lithos*, *264*, 441–452. https://doi.org/10.1016/j.lithos.2016.09.007

Miller, S. A., van der Zee, W., Olgaard, D. L., & Connolly, J. A. D. (2003). A fluid-pressure feedback model of dehydration reactions: Experiments, modelling, and application to subduction zones. *Tectonophysics*, *370*(1), 241–251. https://doi.org/10.1016/S0040-1951(03)00189-6

Moreno, M., Haberland, C., Oncken, O., Rietbrock, A., Angiboust, S., & Heidbach, O. (2014). Locking of the Chile subduction zone controlled by fluid pressure before the 2010 earthquake. *Nature Geoscience*, *7*(4), 292–296. https://doi.org/10.1038/ngeo2102

Padrón-Navarta, J. A., Sánchez-Vizcaíno, V. L., Hermann, J., Connolly, J. A. D., Garrido, C. J., Gómez-Pugnaire, M. T., & Marchesi, C. (2013). Tschermak's substitution in antigorite and consequences for phase relations and water liberation in high-grade serpentinites. *Lithos*, *178*, 186–196. https://doi.org/10.1016/j.lithos.2013.02.001

Padrón-Navarta, J. A., Tommasi, A., Garrido, C. J., Sánchez-Vizcaíno, V. L., Gómez-Pugnaire, M. T., Jabaloy, A., & Vauchez, A. (2010). Fluid transfer into the wedge controlled by high-pressure hydrofracturing in the cold top-slab mantle. *Earth and Planetary Science Letters*, *297*(1), 271–286. https://doi.org/10.1016/j.epsl.2010.06.029

Piccoli, F., Ague, J. J., Chu, X., Tian, M., & Vitale Brovarone, A. (2021). Field-based evidence for intra-slab high-permeability channel formation at eclogite-facies conditions during subduction. *Geochemistry, Geophysics, Geosystems*, *22*(3), e2020GC009520. https://doi.org/10.1029/2020GC009520

Plümper, O., John, T., Podladchikov, Y. Y., Vrijmoed, J. C., & Scambelluri, M. (2017). Fluid escape from subduction zones controlled by channel-forming reactive porosity. *Nature Geoscience*, *10*(2), 150–156. https://doi.org/10.1038/ngeo2865

Powell, R., & Holland, T. (1999). Relating formulations of the thermodynamics of mineral solid solutions; activity modeling of pyroxenes, amphiboles, and micas. *American Mineralogist*, *84*(1–2), 1–14. https://doi.org/10.2138/am-1999-1-201

Räss, L., Duretz, T., & Podladchikov, Y. Y. (2019). Resolving hydromechanical coupling in two and three dimensions: Spontaneous channelling of porous fluids owing to decompaction weakening. *Geophysical Journal International*, *218*(3), 1591–1616. https://doi.org/10.1093/gji/ggz239

Rüpke, L., Morgan, J. P., Hort, M., & Connolly, J. A. D. (2004). Serpentine and the subduction zone water cycle. *Earth and Planetary Science Letters*, *223*(1), 17–34. https://doi.org/10.1016/j.epsl.2004.04.018

Scambelluri, M., Müntener, O., Hermann, J., Piccardo, G. B., & Trommsdorff, V. (1995). Subduction of water into the mantle: History of an Alpine peridotite. *Geology*, *23*(5), 459–462. https://doi.org/10.1130/0091-7613(1995)023<0459:sowitm>2.3.co;2

Scambelluri, M., Pettke, T., Rampone, E., Godard, M., & Reusser, E. (2014). Petrology and trace element budgets of high-pressure peridotites indicate subduction dehydration of serpentinized mantle (Cima di Gagnone, Central Alps, Switzerland). *Journal of Petrology*, *55*(3), 459–498. https://doi.org/10.1093/petrology/egt068

Scambelluri, M., Strating, E. H. H., Piccardo, G. B., Vissers, R. L. M., & Rampone, E. (1991). Alpine olivine- and titanian clinohumite-bearing assemblages in the Erro-Tobbio peridotite (Voltri Massif, NW Italy). *Journal of Metamorphic Geology*, *9*(1), 79–91. https://doi.org/10.1111/j.1525-1314.1991.tb00505.x

Schmidt, M. W., & Poli, S. (1998). Experimentally based water budgets for dehydrating slabs and consequences for arc magma generation. *Earth and Planetary Science Letters*, *163*(1), 361–379. https://doi.org/10.1016/S0012-821X(98)00142-3

Skarbek, R. M., & Rempel, A. W. (2016). Dehydration-induced porosity waves and episodic tremor and slip. *Geochemistry, Geophysics, Geosystems*, *17*(2), 442–469. https://doi.org/10.1002/2015GC006155

Spandler, C., Pettke, T., & Rubatto, D. (2011). Internal and external fluid sources for eclogite-facies veins in the Monviso meta-ophiolite, Western Alps: Implications for fluid flow in subduction zones. *Journal of Petrology*, *52*(6), 1207–1236. https://doi.org/10.1093/petrology/egr025

Spear, F. S. (1993). *Metamorphic phase equilibria and pressure-temperature-time paths*. Mineralogical Society of America.

Spiegelman, M., Kelemen, P. B., & Aharonov, E. (2001). Causes and consequences of flow organization during melt transport: The reaction infiltration instability in compactible media. *Journal of Geophysical Research*, *106*(B2), 2061–2077. https://doi.org/10.1029/2000jb900240

Taetz, S., John, T., Bröcker, M., & Spandler, C. (2016). Fluid–rock interaction and evolution of a high-pressure/low-temperature vein system in eclogite from New Caledonia: Insights into intraslab fluid flow processes. *Contributions to Mineralogy and Petrology*, *171*(11), 90. https://doi.org/10.1007/s00410-016-1295-z

Ulmer, P., & Trommsdorff, V. (1995). Serpentine stability to mantle depths and subduction-related magmatism. *Science*, *268*(5212), 858–861. https://doi.org/10.1126/science.268.5212.858

van Keken, P. E., Hacker, B. R., Syracuse, E. M., & Abers, G. A. (2011). Subduction factory: 4. Depth-dependent flux of H_2O from subducting slabs worldwide. *Journal of Geophysical Research*, *116*(B1), B01401. https://doi.org/10.1029/2010JB007922

Vrijmoed, J. C., & Podladchikov, Y. Y. (2022). Thermolab: A thermodynamics laboratory for nonlinear transport processes in open systems. *Geochemistry, Geophysics, Geosystems*, *23*(4), e2021GC010303. https://doi.org/10.1029/2021gc010303

Watson, E. B., & Wark, D. A. (1997). Diffusion of dissolved SiO_2 in H_2O at 1 GPa, with implications for mass transport in the crust and upper mantle. *Contributions to Mineralogy and Petrology*, *130*(1), 66–80. https://doi.org/10.1007/s004100050350

Wilson, C. R., Spiegelman, M., van Keken, P. E., & Hacker, B. R. (2014). Fluid flow in subduction zones: The role of solid rheology and compaction pressure. *Earth and Planetary Science Letters*, *401*, 261–274. https://doi.org/10.1016/j.epsl.2014.05.052